Forbidden Coronal Iron Line Emission In the Puppis A Shock Front: The Effect of Inhomogeneities

by

Richard G. Teske[1]
Department of Astronomy
The University of Michigan

and

Robert Petre
NASA
Goddard Space Flight Center

[1]Visiting Astronomer, Cerro Tololo Inter-American Observatory, National Optical Astronomy Observatories, operated by AURA, Inc. under contract with the National Science Foundation.

ABSTRACT

We have obtained CCD images of the shock front at the eastern rim of Puppis A in [Fe X] λ6374 and [Fe XIV] λ5303 and have compared the optical data to *Einstein* HRI soft X-ray data. The observed part of the remnant is complex, containing density irregularities. Optical and X-ray data are consistent in showing a nearly flat gradient of ionization behind the shock. To determine conditions in the shock, scans of surface brightness across it in the optical lines were compared to surface brightnesses predicted by idealized Sedov models. We were unable to match both the red and green line scans by a simple, single-component model, and have ascribed the failure to the presence of the density inhomogeneities. Our result has important implications for the determination of SNR shock front models by means of fitting X-ray data with Sedov models.

I. INTRODUCTION

An understanding of the structure of shock fronts in supernova remnants (SNR) has been the subject of extensive observational efforts (see, for example, the reviews by Chevalier [1977], McKee and Hollenbach [1980], and Raymond [1984]). This paper describes an attempt to apply to the Puppis A remnant still another method for determining the physical conditions in a shock: comparison of observed surface brightness profiles across the shock front of the forbidden coronal iron line emission in [Fe X] λ6374 and [Fe XIV] λ5303 with spatially resolved models of the emission distribution. Under conditions of ionization equilibrium the lines are emitted principally in the temperature range $5.9 < \log T < 6.5$, corresponding to shock speeds $250 < V_s < 500$ km s^{-1} that are normally encountered in middle-aged, adiabatic SNR. Higher temperature gas resulting from greater shock speeds is also observable in the lines if the iron is underionized.

Because the ionization length $V_s t_{ionization}$ for the Fe lines is long ($t_{ionization} \cong 1000$ yr for Fe XIV when $n_e = 1$ cm^{-3}), their intensity distribution across a shock front is observationally resolvable in the nearer SNR by means of images secured with a CCD behind interference filters. The images presently can resolve 10" (Teske and Kirshner 1985) or better (Teske 1985; Teske and Petre 1986). Models (Teske 1984) have predicted the lines' radial surface brightness distribution behind a spherical shock front, taking into account time-dependent ionization (i) when T_{ion} and $T_{electron}$ are equilibrated on a time-scale shorter than the the ionization time, and (ii) when Coulomb equilibration of electron energies on the ions dominates (Raymond *et al* 1983). In the spherical blast wave models, the relative intensities of the red and green forbidden lines reflect the equilibration process: for a given shock speed the green line is less intense, and the red line

more intense, when Coulomb equilibration operates, than when temperatures are rapidly equilibrated. Also, the detailed surface brightness distribution of the green line emission is a good diagnostic of shock speed V_s and ambient particle density n_o; the peak line intensity in the shock front goes as n_o^2, while the shape of the brightness distribution behind the shock reflects V_s. Typical scale lengths just behind the shock front for the predicted surface brightnesses are in the range $0.01 \leq l/R_{SNR} \leq 0.05$, or roughly 10^{18} cm = 0.3 pc in middle-aged objects with V_s in the range which will emit observable amounts of the forbidden iron radiation. This length is reasonably resolvable under even indifferent observing conditions in remnants no more distant than a few kpc, using present methods.

We here report on the observation of both the Fe lines at the eastern rim of the Puppis A SNR and application of the data to investigation of conditions in the shock front there. The observations were made for another purpose - to investigate the evaporation of the "eastern X-ray knot" (Teske and Petre 1986; henceforth TP) - at a location in the remnant that is complex and highly structured, containing numerous small density irregularities. An issue that can be examined with the present data is whether, in the presence of the small density fluctuations, the spatially-averaged emission from the shock can be represented by a simple model for shock propagation into a uniform medium, for which "average" values of parameters apply.

To address this issue we have compared the Puppis A iron line observations with *Einstein* HRI soft X-ray observations for the same location on the shock front, and find that the two sets of data are consistent with one another (§IIIb). However, it is not possible to reproduce the observed spatially-averaged Fe surface brightnesses with a simple, single-component blast wave model (§IIIc). These results have important implications for the

determination of single-component shock models of SNR by means of X-ray spectra (§IV).

II. THE IRON LINE OBSERVATIONS

The eastern X-ray knot in Puppis A has been discussed in detail by Petre *et al* (1982; henceforth PCKW). Optical iron line images of its vicinity were made at the CTIO 1.5 m reflector in January 1985 using a low noise CCD behind three-cavity interference filters. One hour exposures were calibrated (by making short exposures on some of Cochran's [1981] spectrophotometric standards) and combined to form single composite images: 12 exposures in λ5303 were co-added, and 9 in λ6374, to assemble the final data frames. The photometric accuracy of the final frames is better than 20% (TP). After sky subtraction, de-reddening, and correction for Paschen continuum contamination on the locations of bright clouds, the scenes were Wiener filtered to improve their signal/noise characteristics. The scale of the images is 1.18" per pixel. In the final pictures, profiles of faint stars have a FWHM of 2.6". Details of data-taking and data reduction are given by TP.

The distance to Puppis A and the column density towards it are not well known. Estimates of the latter cited by TP indicate it to be in the range $1 \times 10^{21} \leq N_H \leq 20 \times 10^{21}$ cm^{-2}. We believe the most reliable guide to the column density is the solution obtained from an analysis of an *Einstein* FPCS spectrum of the eastern knot by Winkler *et al* (1981); their results are consistent with $2 \times 10^{21} \leq N_H \leq 6 \times 10^{21}$ cm^{-2}. We have selected $N_H = 4 \times 10^{21}$ cm^{-2} and assumed it to be uniform across our field of view. With the relation between extinction and column density obtained from Jenkins and Savage (1974) we calculate $A_V = 1.7$. Our values are similar to those used by Winkler and Kirshner (1985) who adopted

$N_H = 3 \times 10^{21}$ cm^{-2} and computed $A_V = 1.5$ for the remnant. We have taken the distance to it to be 2 kpc (Downes 1971; Milne 1979).

III. RESULTS

a. The Observed Surface Brightness Profiles in Puppis A.

In Figure 1 we show the λ5303 image of the eastern part of Puppis A overlaid by contours of PCKW's *Einstein* HRI soft X-ray data. Scans of surface brightness in the Fe lines and in the X-rays along a radius of the remnant were obtained from the northern part of Figure 1, north of $\delta = 42°46'46"$ (indicated on the Figure), where a radius of the remnant runs nearly EW on the sky. The resulting profiles are shown in Figure 2. Each data point of the X-ray scan is the average of counts in rectangles of dimensions 52" NS x 4" EW; the Fe scans average intensities in rectangles 82" NS x 1.2" EW. In the Figure the abcissae are in arcminutes on the sky as distinguished from arcminutes of right ascension measured along the equator, and the zero point is placed to mark approximately the mean location of the X-ray edge, thus presumably the position of the shock front. The forbidden iron intensities in the Figure have been corrected for reddening, while the X-ray scan remains uncorrected. Typical one-sigma error bars are shown.

In Figure 2c the rise of the [Fe X] red line intensity to the eastward - to the left of - the shock front is due to a low level of reflected light from the surface of the red filter at the extreme edge of the field of the λ6374 images. We have carefully studied all the images and find no other evidence of parasitic light in them.

b. The Problem.

The almost steady rise of λ6374 surface brightness behind the shock front towards the west - to the right in Figure 2c - implies a decreasing degree of iron ionization towards the remnant interior and is thus unexpected and in conflict with predictions of Sedov-Taylor blast wave models (Teske 1984), which show an increasing degree of ionization towards the remnant interior. The prediction does not depend on accomplishment of ionization equilibrium or upon the process by which ion and electron energies are equilibrated. We note that the soft X-ray surface brightness in Figure 2 begins to increase somewhat to the east of the first rise in λ5303 intensity, while the λ6374 red line brightness begins to rise still further westward of λ5303 - farthest into the remnant's interior - also suggesting a decreasing degree of ionization behind the shock.

c. The Degree of Iron Ionization Behind the Shock.

To explore the changing degree of iron ionization behind the shock we have computed two observed ionization indices composed of the point-to-point ratios $I_{\lambda 5303}/I_{\lambda 6374}$ and $I_{\lambda 5303}/$(X-ray Cts). Figure 3 shows the observed spatial distribution of the ratios. The former is computed from the de-reddened intensities, the latter from the corrected optical intensity and the uncorrected X-ray counts. The Fe/Fe ratio was derived by first smoothing the point-to-point data of Figure 2 with five data-point averages, while the Fe/X-ray ratio relies on a hand-smoothed profile of the green line intensity. These observed ratios may be examined with the help of theoretical intensity ratios for ionization equilibrium given in Table 1.

Emissivities for the Fe lines were computed from atomic data

given by Mason (1975) and by Malinovsky, Dubau, and Sahal-Brechot (1980) taking due account of proton excitation and the effects of cascades. For the $I_{\lambda 5303}$/(X-ray Cts) index we adopted log A_{Fe} = 7.4 by number, where log H = 12, and used the emission measure per unit HRI surface brightness from Figure 6 of PCKW for $N_H = 4 \times 10^{21}$ cm^{-2}, taking the X-ray exposure time into account. Thus the interstellar extinction of the X-rays, for which no correction was made in treating the observed data, has been folded into the theoretical values for direct comparison with the observations.

The observed [Fe XIV]/[Fe X] ratio behind the shock ranges around 5. to 0.5 (Figure 3b), corresponding to a decline of around 0.1 dex in temperature if ionization equilibrium conditions hold there (Table 1), and thus implying a nearly constant degree of iron ionization. Further, the Fe/X-ray ratio remains at levels near 6 to 10 x 10^{-8} erg cm^{-2} s^{-1} sr^{-1} Ct^{-1}, also implying nearly constant ionization conditions behind the shock (c. f. Table 1). If the remnant were isothermal (Solinger, Rappaport, and Buff 1975) the surface brightnesses of both optical lines and X-rays would show the same overall spatial distribution, something not observed in this case, so that it is unlikely the remnant is in fact strictly isothermal. Since ionization equilibrium probably does not hold just behind the shock (Winkler, Canizares, and Bromley 1983; Szymkowiak 1985) we cannot determine temperatures from our data and prefer only to conclude that the observed indices [Fe XIV]/[Fe X] and [Fe XIV]/(X-ray Cts) are consistent with one another in indicating a nearly flat radial gradient of Fe ionization behind the shock in the locality being studied, rather than the increasing ionization expected from Sedov-Taylor models.

The conclusion is essentially independent of the adopted reddening correction; the actual values of the ratios shown in Figure 3 will change by less than a factor of two for N_H in the favored range 2 x 10^{21} to 6 x 10^{21} cm^{-2}.

d. Model Surface Brightness Profiles for the Fe Lines.

To appraise the magnitude of the conflict between theory and observation we have computed radial distributions of red and green line intensities for Sedov-Taylor models using the code developed by Teske (1984). The calculations show the conflict to be severe.

A good match can be achieved for the de-reddened green line data with parameters (see Table 2) for the blast wave models near to those obtained by others (e. g. Szymkowiak 1985). The best match is obtained if we arbitrarily assume the shock front lies at right ascension $\alpha = 8^h22^m33.0^s$, a location some 30" to 40" west of the X-ray edge. Figure 4 shows the comparison between observation and theory for model parameters given in Table 2.

These models predict that the red line reaches a peak intensity of 0.2×10^{-7} erg cm^{-2} $s^{-1}sr^{-1}$ just behind the shock front, its surface brightness decreasing towards the remnant interior. The observed λ6374 intensities actually increase towards the west (Figure 2c), reaching a peak at least 20 times the model values.

IV. DISCUSSION

a. The Effect of Changing the Reddening Correction.

The conflict between observation and theory is not ascribable to a wrong choice of reddening correction. For the adopted value of $A_V = 1.7$, the Fe line extinction factors are 3.50 for λ6374, and 5.15 for λ5303. Since the discrepancy for the λ6374 red line is the factor $I_{corrected}/I_{predicted} \cong 20$, the discrepancy cannot be eliminated even by postulating a zero column density towards Puppis A, for the following reason. Because the calculated surface brightness of blast wave models goes as n_o^2, the removal of the

reddening correction from the λ5303 data decreases by a factor $5.15^{1/2}$ the n_o needed to match them and thus decreases the predicted λ6374 intensity by the same factor. Upon removal of the reddening correction from the λ6374 data (a factor of 1/3.50), the discrepancy factor then becomes 13 instead of 20, leaving the observed λ6374 intensity still an order of magnitude too high in comparison with the models. Further, adoption of a still greater extinction will only increase the discrepancy.

In neither case is the *gradient* of $I_{\lambda 6374}$ behind the shock affected by a change in reddening correction. But a differential extinction across the remnant, lessening towards the west, cannot be invoked to explain the westward gradient of $I_{\lambda 6374}$ for two reasons. First, an evident gradient of λ5303 intensity should then be seen since the green line will be more greatly affected, but this is not clearly present. Second, the required extinction gradient, at least 3 magnitudes (2.5 log 20) across two or three arcminutes, is not evident in the numbers of stars seen to be located in different places on the CCD frames (TP).

b. The Role of Density Inhomogeneities.

The problem is likely caused by the operation in the observed region of one or more mechanisms not modelled by the blast wave code (which already includes non-equilibrium ionization and a choice of either rapid or Coulomb equilibration of ion and electron energies). We speculate that the mechanism(s) is associated with inhomogeneities which are seen in the region.

PCKW noted distinct surface brightness irregularities down to 12" size in their X-ray data; the features are clearly seen in their Figure 7, and appear to be bright structures superposed on a fairly uniform background. Since the HRI instrument responds more sensitively to density fluctuations than to temperature

fluctuations in the range of temperatures at which the optical forbidden lines are formed, we can conclude - as did PCKW - that the brightness fluctuations correspond to local density enhancements. Our forbidden line images of the region also show muted local intensity fluctuations on a scale around 10"; these cannot be as definitely ascribed to density effects since the emissivities of both Fe lines are also strongly temperature sensitive. We therefore rely on the X-ray data as showing density enhancements in the region.

The enhancements above "background" of the X-ray surface brightness fluctuations are in the range 20% to 80%, thus representing density increments of factors roughly $\sqrt{1.2}$ to $\sqrt{1.8}$, and they are seen on a scale of 12" to 16" (approximately 0.1 pc to 0.15 pc). Some 15 to 20 of the features can be identified in the region north of the λ5303 cloud and X-ray knot, spread across a projected area of about 0.9 pc x 0.7 pc. These gentle irregularities are clearly distinguishable from clouds on the basis of their density and size. In order to be considered clouds as such, their density contrast with the surrounding medium should be a factor of 10 or more. Further, if the features were indeed clouds having the observed small dimensions they would already have evaporated into the hot, low-density remnant interior (PCKW). It is likely that these weak density enhancements are in pressure equilibrium with their surroundings.

The density irregularities existed in the region prior to the shock's arrival, and their presence has influenced its overall propagation. Once they are swept up by it, shock heating plus (potentially) subsequent evaporation can importantly modify the emission measure behind the front in the intercloud medium, and thus its observed properties.

We have not modelled the encounter between shock front and density irregularities. However, a numerical investigation by Sgro

(1975) of a shock/cloud interaction can be drawn upon to test the plausibility of the notion that the visible density irregularities are responsible for the apparent ionization gradient. Sgro's (1975) model applies if we view the shock's encounter with the inhomogeneities as occurring between a shock and cold cloud.

While the shock is still traversing a denser feature, the density contrast with the surroundings is preserved from pre-encounter times. If the density structures which we see just behind the shock are still shocked, then (in Sgro's [1975] notation, where subscript c refers to the cloud):

$$(1.2)^{-1/2} \leq \frac{n}{n_c} \leq (1.8)^{-1/2}$$

$$1.05 \leq \beta \leq 1.21, \quad 0.93 \leq \frac{V_c}{V} \leq 0.98, \quad 0.86 \leq \frac{T_c}{T} \leq 0.95,$$

since the post-shock temperature depends on V^2.

The expected temperature or ionization contrast of the density features is then seen to be small. The radiation that they contribute to our declination-averaged surface brightness scans will contain brighter [Fe X] emission than in the intercloud shock, as the observations require, and potentially could lead to the apparent observed small inward change of average Fe ionization implied by the forbidden iron data. Farther behind the shock the inhomogeneities are probably re-expanding (Sgro 1975). Since it is not likely that there has been enough time for recombination to have had a great effect on the Fe ionization in them, their overall ionization contrast also should be small. While these considerations make plausible the interpretation that shocked density irregularities are responsible for our observation, confirmation will require a complete gas-dynamic calculation.

Whether evaporation also plays an important role remains open to question. Teske and Kirshner (1985) believe they have observational evidence for it in the Cygnus Loop, while Hester and

Cox (1986) argue that this interpretation is erroneous. A simple model of evaporative flow (Teske and Petre 1986) provides a quantitative match for many observed characteristics of the Puppis A λ5303 cloud (Figure 1). However, models of non-equilibrium evaporative flows from clouds, constructed by Ballet, Arnaud, and Rothenflug (1986), have raised serious questions about evaporation theories. One expects that evaporation will be most strongly driven when large density variations ("clouds") are present. Because the density irregularities at the observed Puppis A site are gentle ones, evaporation may not be important or even relevant.

Evidently the source volume behind the Puppis A shock front contains significant amounts of gas in a lower Fe ionization state than our blast wave models allow. Our declination-averaged observations depict a composite radiation from regions of varying density and temperature which does not exhibit the characteristics of emission from a uniform medium of "average" properties. Much more interesting is the corollary of this proposition, that if inhomogeneities are present, the usual synthesis approach to analysis of shock front data - for example through study of X-ray spectra - does not necessarily lead to reliable specification of ambient density or shock speed. Thus our negative result may have important implications for the study of non-radiative shocks.

In the present instance of density irregularities behind the Puppis A shock front, independent of whether the material is entirely the result of shock heating of density enhancements within an inhomogeneous medium, or whether evaporative processes involving the inhomogeneities might also be making a contribution, the lower ionization gas has demonstrated its presence by modifying the surface brightness distribution of the optical forbidden lines. Although we have been able to achieve a match of a model to the green line information, the fit is likely a

fortuitous one: the composite emission from behind the shock front has likely falsified the λ5303 intensities as well. An indication of this is that, to get a match, we require a slower shock speed than anyone else has ever published for the remnant (Table 2).

c. Summary

The problem posed here has been the determination of physical conditions in the Puppis A shock front through modelling of the observed, declination-averaged, optical forbidden line intensities with a single-component blast wave. In principle, the approach we followed - fitting a model to data obtained from photometrically calibrated pictures taken in the forbidden Fe lines - has no extra degrees of freedom, although we allowed one: the arbitrary specification of the shock front location as seen in the green line. Because the distance to the SNR is uncertain and its projected outline non-circular, another degree of adjustment (of R_{SNR}) is available for the Puppis A remnant. The approach is a powerful one since it requires fitting two separate spatial distributions of forbidden iron line data points by a single model: it places strong constraints upon a plausible physical description of the emitting source volume. Although it is possible to reproduce the mean radial surface brightness distribution of the green line with an idealized Sedov model, we have been unable to match all the observations (including the red line data) with a single model, and have speculated that the failure to do so can be traced to the inhomogeneous structure of the ISM at the location of the observations.

Had we, for example, measured only the total flux in each Fe line from some single area behind the shock it would be easily possible - because of the much weaker constraints- to construct a simple blast wave model that would indeed match the two area-averaged flux data points.

Hamilton and Sarazin (1984) studied the bulk X-ray emission from Sedov models and concluded that the spatially-integrated emission from the whole remnant, in the presence of a statistically homogeneous distribution of density inhomogeneities, can be characterized by a simple model of propagation into a smooth medium by a suitable choice of characteristic average ionization time and average temperature. But, as they pointed out, spatial imaging of parts of remnants in X-rays potentially can distinguish the effects of inhomogeneities or other departures from an idealized Sedov model. The question is whether the fixing of model parameters from the process of fitting idealized model to data will yield meaningful values of parameters that physically characterize in an accurate way the remnant being investigated. The potentially high spatial resolution of the optical forbidden iron data can be an important guide in this respect.

In the Puppis A shock front near the eastern X-ray knot we have found that the spatial distributions of $I_{\lambda 5303}/I_{\lambda 6374}$ and $I_{\lambda 5303}$/(HRI X-Ray Cts) both give a consistent general picture of ionization with distance behind the shock. Thus if the optical iron line data cannot be fitted by an idealized Sedov model for a smooth ISM having "average" values of V_s and n_o, the fitting of X-ray spectra to such models might possibly be misleading. Further observations and careful testing of this notion are greatly desirable.

TABLE 1

Theoretical Intensity Ratios for Equilibrium Ionization

Log T	$\frac{I_{\lambda 5303}}{I_{\lambda 6374}}$	$\frac{I_{\lambda 5303}}{\text{HRI X-Ray Counts}}$ erg cm^{-2} s^{-1} sr^{-1} Ct^{-1}
6.0	5.5×10^{-4}	0.08×10^{-8}
6.1	2.8×10^{-3}	3.4×10^{-8}
6.2	0.084	$50. \times 10^{-8}$
6.3	1.7	$190. \times 10^{-8}$
6.4	28.	$63. \times 10^{-8}$
6.5	360.	5.8×10^{-8}
6.6	-	0.6×10^{-8}
6.7	-	0.06×10^{-8}

TABLE 2

Parameters for the Sedov Models Which Were Used to Compute the λ5303 Surface Brightnesses in Figure 4.

Figure	Case	V_s (km/s)	n_o (cm^{-3})	Age (yr)	Radius (pc)
4a	Rapid Equilibration	375	0.32	14,600	14
4b	Coulomb Equilibration	390	0.31	14,000	14

REFERENCES

Chevalier, R. A. 1977, *Ann. Rev. Astr. Ap.*, **15**, 175.

Cochran, A. L. 1981, *Ap. J. Suppl.*, **45**, 83.

Downes, D. 1971, *Astr. J.*, **76**, 305.

Hamilton, A. J. S., and Sarazin, C. L. 1984, *Ap. J.*, **284**, 601.

Malinovsky, M., Dubau, J., and Sahal-Brechot, S. 1980, *Ap. J.*, **235**, 665.

Mason, H. E. 1975, *M. N. R. A. S.*, **170**,651.

McKee, C. F., and Hollenbach, D. J. 1980, *Ann. Rev. Astr. Ap.*, **18**, 219.

Milne, D. K. 1979, *Australian J. Phys.*, **32**, 83.

Petre, R., Canizares, C. R., Kriss, G. A., and Winkler, P. F. 1982, *Ap. J.*, 258, 22 (PCKW).

Raymond, J. C. 1984, *Ann. Rev. Astr. Ap.*, **22**, 75.

Raymond, J. C., Blair, W. P., Fesen, R. A., and Gull, T. R. 1983, *Ap. J.*, **275**, 636.

Sgro, A. G. 1975, *Ap. J.*, **197**, 621.

Solinger, A., Rappaport, S., and Buff, J. 1975, *Ap. J.*, **201**, 381.

Szymkowiak, A. E. 1985, NASA Technical Memorandum 86169 *X-Ray Spectra of Supernova Remnants.*

Teske, R. G. 1984, *Ap. J.*, 277, 832.

Teske, R. G. 1985, *B. A. A. S.*, 17, 596.

Teske, R. G., and Kirshner, R. P. 1985, *Ap. J.*, 292, 22.

Teske, R. G., and Petre, R. 1986, *Ap. J.*, Submitted (TP).

Winkler, P. F., Canizares, C. R., Clark, G. W., Markert, T. H., and Petre, R. 1981, *Ap. J.*, 245, 574.

Winkler, P. F., Canizares, C. R., and Bromley, B. C. 1983, *I.A.U. Symposium No. 101 on Supernova Remnants and Their X-Ray Emission*, eds. J. Danziger and P. Gorenstein (Dordrecht: D. Reidel) pg. 245.

Winkler, P. F., and Kirshner, R. P. 1985, *Ap. J.*, 299, 981.

FIGURE CAPTIONS

Fig. 1 - This optical image in λ5303 of the "eastern X-ray knot" in Puppis A is overlaid by *Einstein* HRI soft X-ray contours at levels 0.95, 4.9, 7.9, 9.9, and 11.9 counts per 4" x 4" pixel. The shock front propagates eastward, towards the left. The line drawn at declination $\delta = -42°46' 46"$ delineates the southern border for the surface brightness scans. The upper edge of the X-ray contours delineates the northern border for the X-ray profile, while the northern border for the optical data profiles extends slightly outside the upper edge of this picture.

Fig. 2 - Declination-averaged profiles across the shock front in Puppis A. The diagrams are spatially aligned and to the same scale. The shock propagates eastward, to the left in these diagrams.

a. Mean HRI X-ray counts per 4" x 4" pixel.

b. Mean λ5303 intensities. The data have been de-reddened. Typical one-sigma error bars are shown.

c. Mean λ6374 intensities. The data have been de-reddened. In this panel the rise towards the east - towards the left side of the diagram at negative values of the abcissa - is spurious and caused by a patch of weakly-reflected light. There is no other evidence of parasitic light in the data. Typical

one-sigma error bars are shown.

Fig. 3 - Ratios of (*a*) $I_{\lambda 5303}$/(HRI X-Ray Cts) and (*b*) $I_{\lambda 5303}/I_{\lambda 6374}$ across the shock front. Both panels are spatially aligned and to scale, and the shock moves eastwards, towards the left. The ordinate scale in (*a*) is in units of 10^{-8}erg cm^{-2} s^{-1} sr^{-1} Ct^{-1} ; theoretical values for the ratio are found in Table 1. The curve in (*a*) was obtained from HRI data *uncorrected* for extinction and a *hand-smoothed* version of the $I_{\lambda 5303}$ curve of Figure 2*b*. The curve in (*b*) here was obtained by smoothing the de-reddened iron data in five-row segments, representing 4.9" in the EW direction. The large jump is located at a place where the average λ6374 intensity is nearly zero.

Fig. 3 - The observed declination-averaged λ5303 scan is here fitted by idealized Sedov models whose parameters are listed in Table 2.

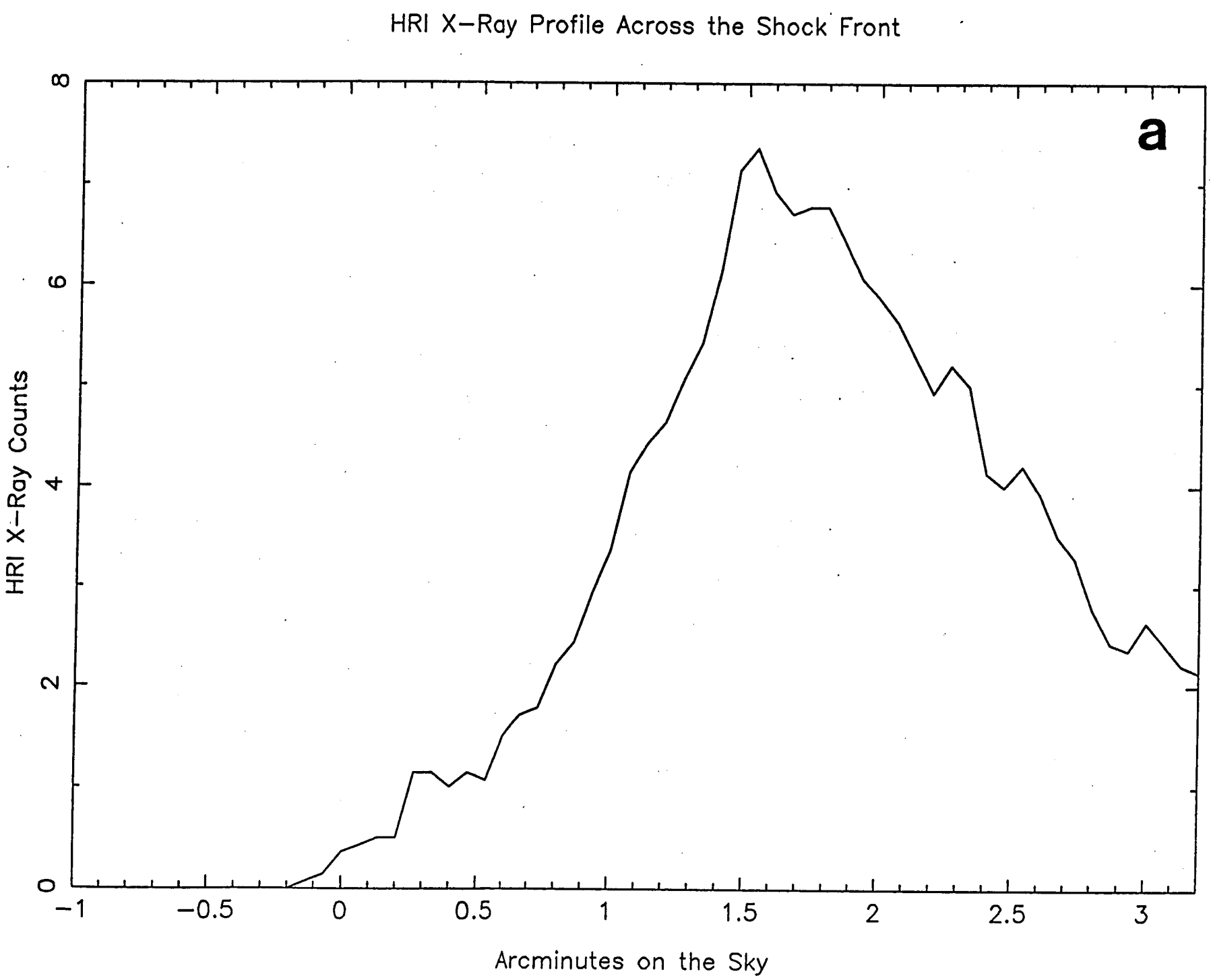
HRI X-Ray Profile Across the Shock Front
a
HRI X-Ray Counts
0
2
4
6
8
−1
−0.5
0
0.5
1
1.5
2
2.5
3
Arcminutes on the Sky

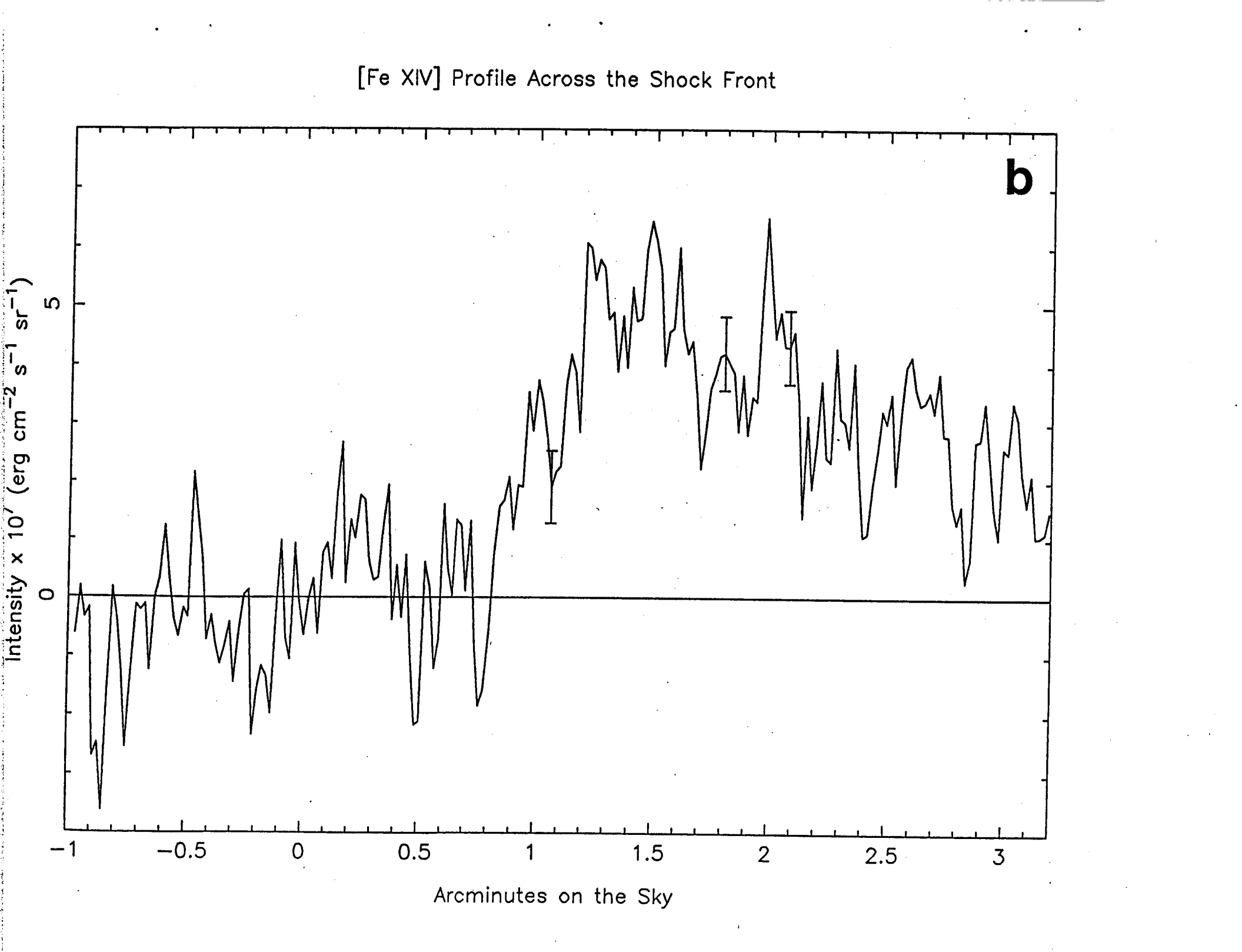
[Fe XIV] Profile Across the Shock Front
b
Intensity x 10⁷ (erg cm⁻² s⁻¹ sr⁻¹)
5
0
−1
−0.5
0
0.5
1
1.5
2
2.5
3
Arcminutes on the Sky

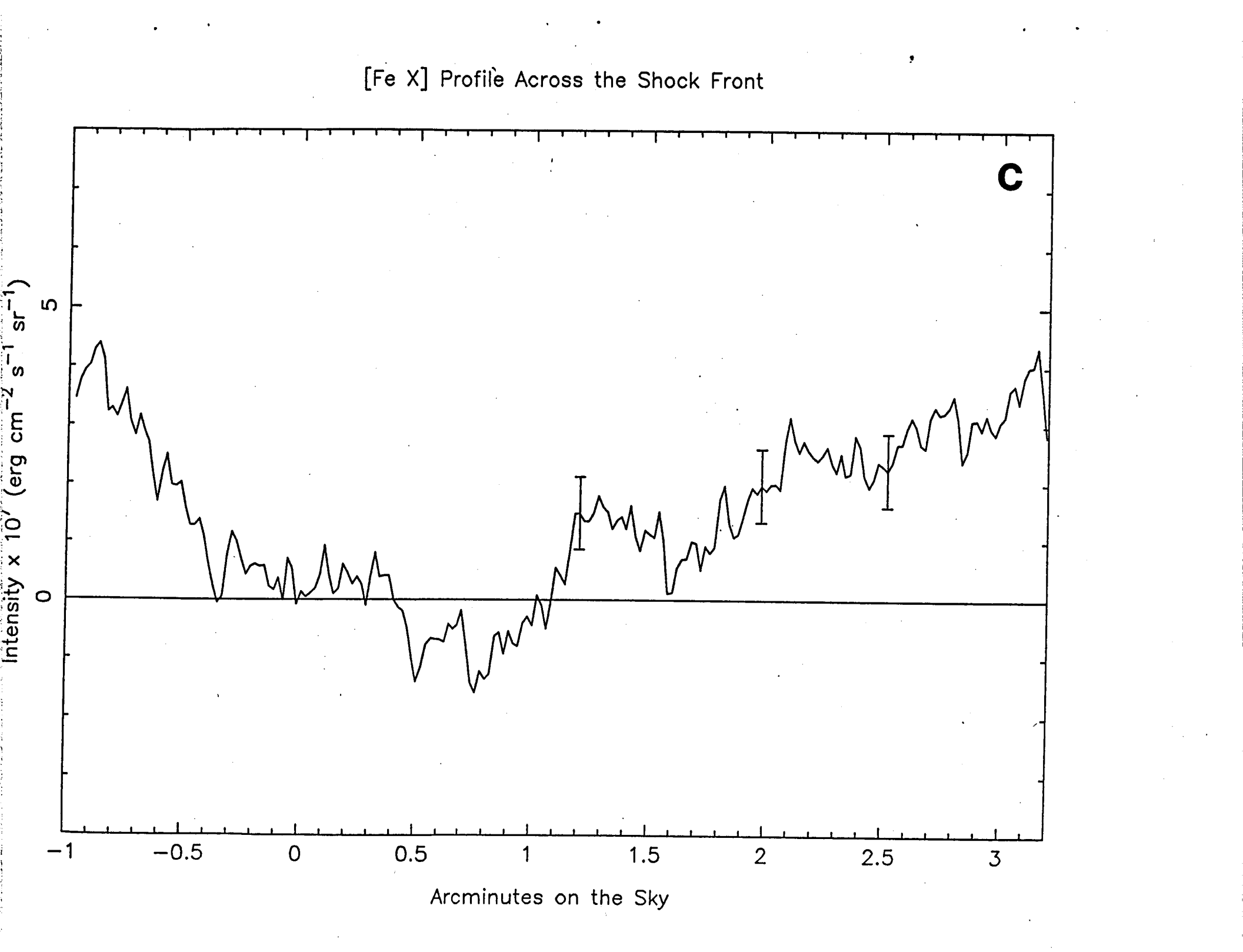
[Fe X] Profile Across the Shock Front
C
Intensity x 10⁷ (erg cm⁻² s⁻¹ sr⁻¹)
5
0
−1
−0.5
0
0.5
1
1.5
2
2.5
3
Arcminutes on the Sky

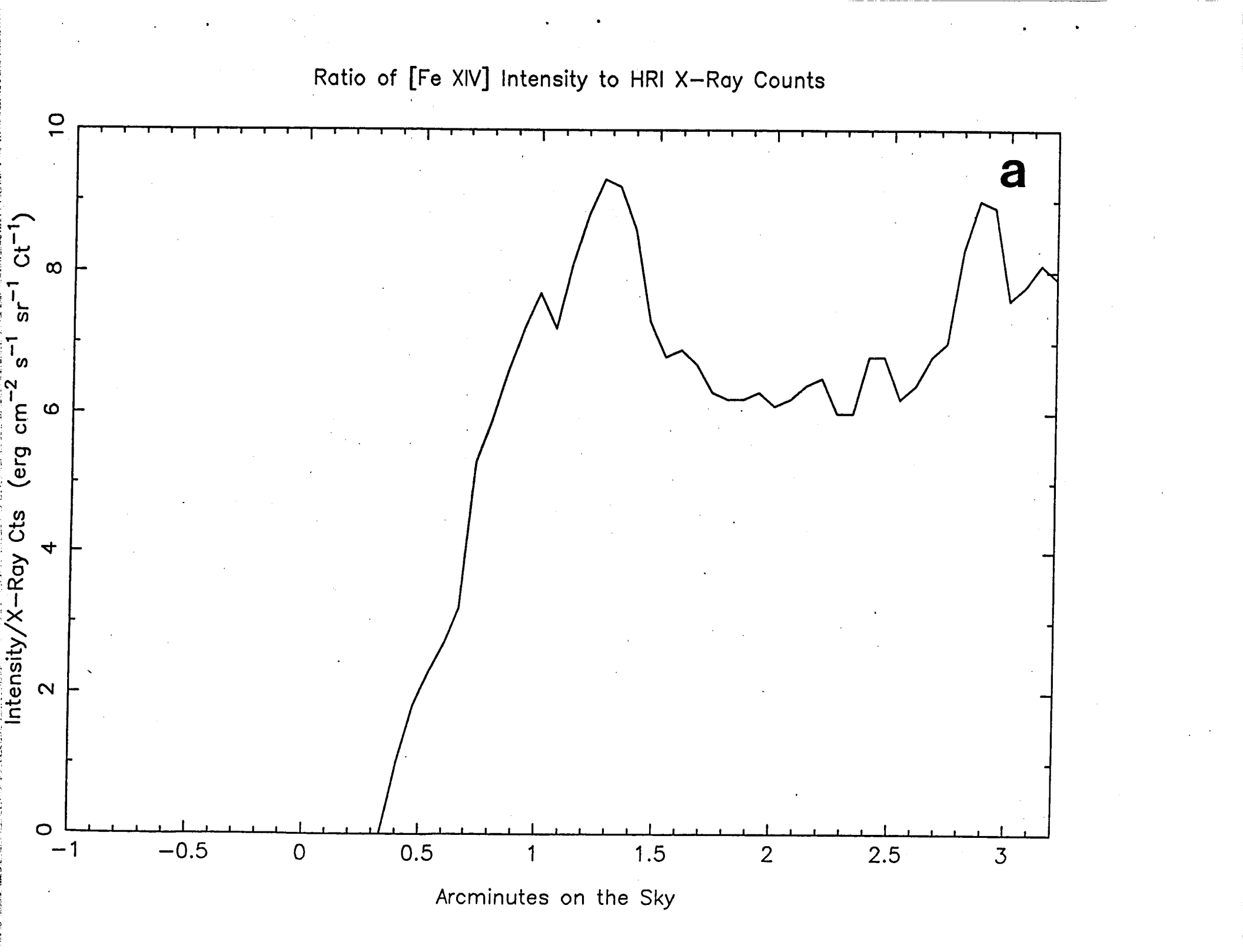
Ratio of [Fe XIV] Intensity to HRI X-Ray Counts
a
Intensity/X-Ray Cts (erg cm^{-2} s^{-1} sr^{-1} Ct^{-1})
0
2
4
6
8
10
−1
−0.5
0
0.5
1
1.5
2
2.5
3
Arcminutes on the Sky

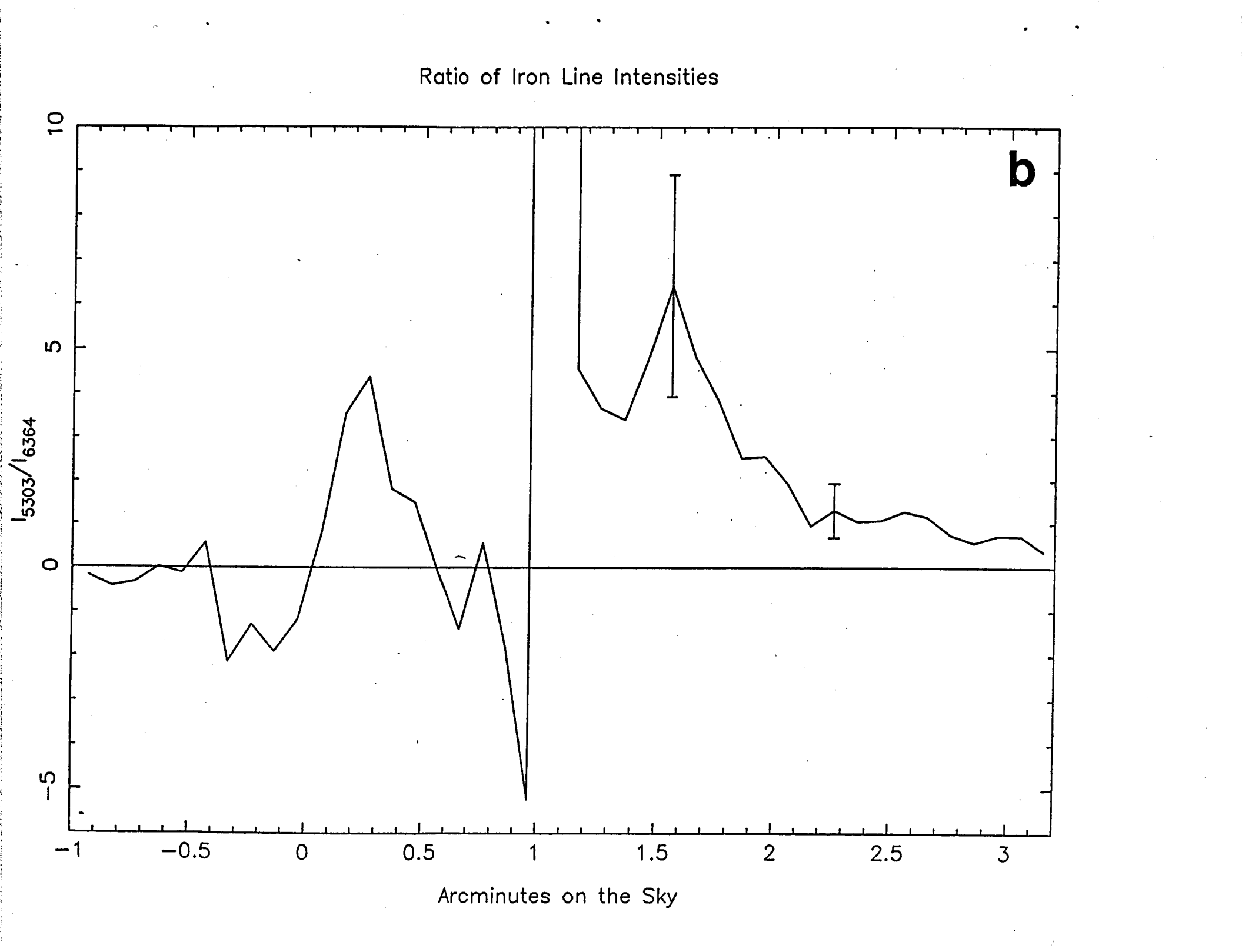
Ratio of Iron Line Intensities
b
I_{5303}/I_{6364}
10
5
0
−5
−1
−0.5
0
0.5
1
1.5
2
2.5
3
Arcminutes on the Sky

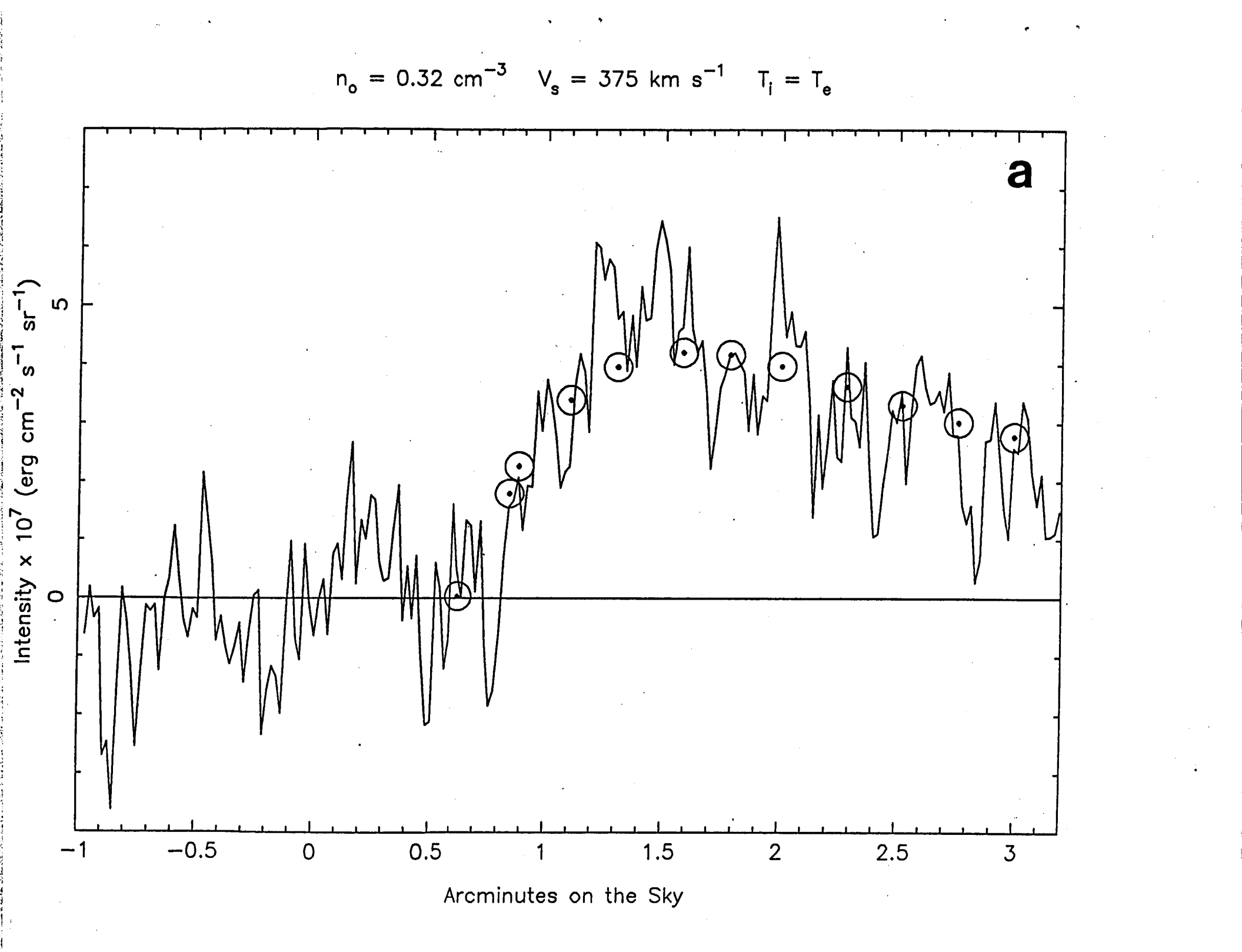
n_o = 0.32 cm^{-3} V_s = 375 km s^{-1} $T_i = T_e$
a
Intensity x 10^7 (erg cm^{-2} s^{-1} sr^{-1})
5
0
−1
−0.5
0
0.5
1
1.5
2
2.5
3
Arcminutes on the Sky

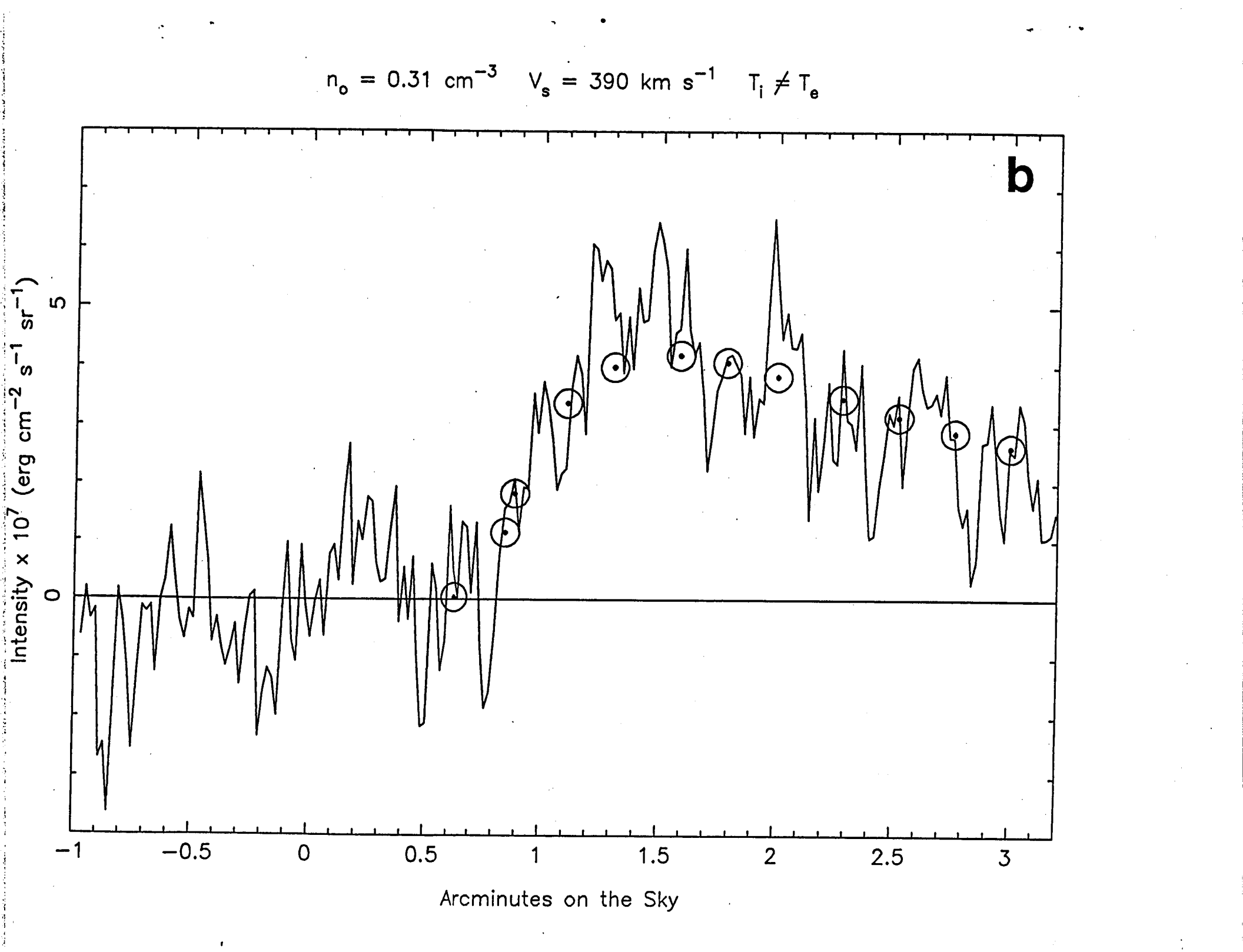
$n_o = 0.31\ cm^{-3}$ $V_s = 390\ km\ s^{-1}$ $T_i \neq T_e$
b
Intensity x 10^7 (erg cm^{-2} s^{-1} sr^{-1})
5
0
−1
−0.5
0
0.5
1
1.5
2
2.5
3
Arcminutes on the Sky